



CHORUS

This is the accepted manuscript made available via CHORUS. The article has been published as:

Effects of ferroelectric polarization on surface phase diagram: Evolutionary algorithm study of the BaTiO₃(001) surface

Pengcheng Chen, Yong Xu, Na Wang, Artem R. Oganov, and Wenhui Duan

Phys. Rev. B **92**, 085432 — Published 28 August 2015

DOI: [10.1103/PhysRevB.92.085432](https://doi.org/10.1103/PhysRevB.92.085432)

Effects of ferroelectric polarization on surface phase diagram: an evolutionary algorithm study of the BaTiO₃(001) surface

Pengcheng Chen^{1,2}, Yong Xu^{1,2,3}, Na Wang^{1,2}, Artem R. Oganov^{5,6,7}, Wenhui Duan^{1,2,4*}

¹*Department of Physics and State Key Laboratory of Low-Dimensional Quantum Physics,*

Tsinghua University, Beijing, 100084, People's Republic of China

²*Collaborative Innovation Center of Quantum Matter,*

Tsinghua University, Beijing 100084, People's Republic of China

³*Department of Physics, McCullough Building,*

Stanford University, Stanford, California 94305-4045, USA

⁴*Institute for Advanced Study, Tsinghua University,*

Beijing 100084, People's Republic of China

⁵*Department of Geosciences, Center for Materials by Design,*

and Institute for Advanced Computational Science,

State University of New York, Stony Brook, NY 11794-2100

⁶*Moscow Institute of Physics and Technology,*

Dolgoprudny city, Moscow Region, 141700, Russian Federation

⁷*Northwestern Polytechnical University, Xi'an, 710072, China*

(Dated: August 13, 2015)

Abstract

We have constructed the surface phase diagram of the $\text{BaTiO}_3(001)$ surface by employing an evolutionary algorithm for surface structure prediction, where the ferroelectric polarization is included as a degree of freedom. Among over 1000 candidate structures explored, a surface reconstruction of $(2\times 1)\text{-TiO}$ is discovered to be thermodynamically stable and have the $p2mm$ plane group symmetry as observed experimentally. We find that the influence of ferroelectric polarization on the surface free energy can be either negligibly small or sizably large (over 1 eV per (2×1) supercell), depending strongly on the surface structure and resulting in a significant distinction of surface phase diagram with varying ferroelectric polarization. It is therefore feasible to control the surface stability by applying an external electric field. Our results may have important implications in understanding the surface reconstruction of ferroelectric materials and tuning surface properties.

PACS numbers: 68.35.B-, 77.80.-e, 05.70.-a, 71.15.Mb

I. INTRODUCTION

The search for stable surface structures is a key subject of surface science and of great importance to fundamental research as well as practical applications, like photovoltaics, catalysis, and sensors¹⁻⁵. Density functional theory (DFT) in combination with *ab initio* thermodynamics is an indispensable tool because of the atomic insight it provides⁶⁻⁸. In this approach, the surface free energy is expressed as a function of stoichiometry and atomic chemical potentials so as to consider the varying growth conditions, and the minimization of the surface free energy predicts stable surface phases. Very recently, the approach has been developed for semiconductors to include the electron chemical potential as a new parameter, which can be generally applied to study the effects of bulk dopants on properties of semiconductor surfaces and interfaces⁴. Further generalization of the approach to other systems would be interesting.

In ferroelectric materials, the ferroelectric polarization couples strongly with the crystal structure, and consequently any change of the ferroelectric polarization will in turn affect the structural stability. Thus, the ferroelectric polarization that can be easily controlled by external electric field is an important degree of freedom for ferroelectric surfaces. However, ferroelectric polarization has hardly been taken into account in the previous calculations of surface phase diagrams of ferroelectric materials. Recent first-principles study indeed showed that surface stability of ferroelectric lithium niobate is different for the positively and negatively polarized surfaces, which is actually driven more by the different surface termination than intrinsic ferroelectric polarization⁹.

As a prototypical ferroelectric material, barium titanate (BaTiO_3 , BTO) plays a vital role in numerous applications and has been intensively studied theoretically.¹⁰⁻¹⁷ As shown in Fig. 1, BTO has a perovskite structure and undergoes a structural transition from high-symmetry cubic phase to low-symmetry tetragonal phase when lowering temperature across ~ 400 K¹⁸. The (001) face is a stable cleavage plane and has rich surface reconstructions, including (1×1) , (2×1) , $c(2 \times 2)$, (2×2) , $(\sqrt{5} \times \sqrt{5})$, (3×1) , (3×2) , and (6×1) periodicities¹⁹⁻²⁴. Among them, the (2×1) reconstruction has recently attracted much attention^{19,25,26}. Two different surface structure models have been proposed. However, one structure model^{19,25} displays the pm plane group symmetry, in contradiction with the $p2mm$ symmetry identified by recent x-ray diffraction experiments²⁶; the other one²⁶ has the correct symmetry but is energetically

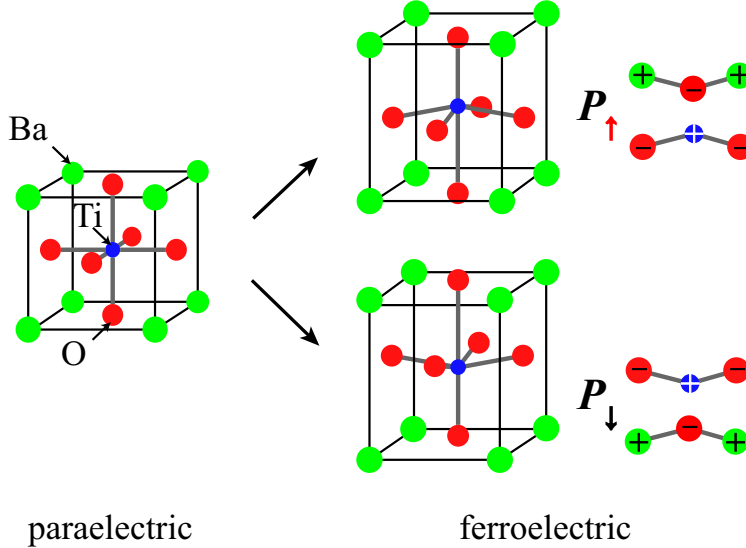


FIG. 1. (Color online) The atomic structure of bulk BaTiO₃ in paraelectric and ferroelectric phase. The polarizations \mathbf{P}_\uparrow and \mathbf{P}_\downarrow are determined by the displacement between O and Ba/Ti along the [001] direction. The green, blue and red balls represent Ba, Ti and O atoms, respectively.

less stable than the former. The actual atomic structure of the BTO(001)-(2 × 1) surface remains elusive.

In this work, we will consider ferroelectric polarization as an extra degree of freedom to calculate surface phase diagram of ferroelectric materials. Specifically, we perform first-principles calculations for the BTO(001) surface, focusing on (2 × 1) as well as (1 × 1) reconstructions to find stable surface configurations and to reveal the effects of ferroelectric polarization. By employing a newly designed evolutionary algorithm²⁷ for efficiently searching (meta)stable configurations and calculating over 1000 possible structure models, we predict a surface phase diagram containing many new surface structures, including a thermodynamically stable (2 × 1)-TiO phase that has the $p2mm$ plane group symmetry observed experimentally²⁶. More importantly, we find that the influence of ferroelectric polarization on the surface free energy can be either negligibly small or sizably large (over 1 eV per (2 × 1) supercell for BTO(001)), depending strongly on the surface structure. As a result, the surface phase diagram changes significantly with varying ferroelectric polarization. These findings suggest a unique way to control surface structures and properties of ferroelectrics.

II. MODELS AND METHODS

First-principles calculations were performed with DFT as implemented in the Vienna *ab initio* simulation package²⁸, using the projector augmented wave method²⁹ and the Perdew-Burke-Ernzerhof (PBE) exchange correlation functional^{30,31}. The method for predicting surface reconstructions was based on an evolutionary algorithm as implemented in the USPEX package³², allowing variable-composition structure searches, where the numbers of atoms in the surface region are varied to yield the global minimum of the surface free energy (see Refs.^{27,33,34} for more details). To demonstrate the effect of ferroelectric polarization on surface reconstructions, we focused on discussing the TiO₂-terminated surfaces, which have been extensively observed experimentally and studied theoretically^{19,24,25}, and considered only an ideal bulk-terminated phase for the BaO-terminated surface. The BTO(001) surfaces were modeled by periodic slabs composed of four -TiO₂-BaO- bilayers plus a TiO₂ termination together with a 15 Å thick vacuum layer³⁵. Different surface stoichiometries were considered by adding a layer of Ti_xO_y ($x=0, 1, 2, y=0, 1, 2, 3, 4$) in a (2 × 1) surface supercell on the otherwise ideal TiO₂-terminated surface. The bottom three bilayers were fixed at their bulk configuration, and the other layers were relaxed using the conjugate gradient algorithm till residual forces were smaller than 0.01 eV/Å². A Monkhorst-Pack k -point mesh with reciprocal-space resolution of $2\pi \times 0.03 \text{ \AA}^{-1}$ and a 400 eV planewave cutoff energy were used. Dipole correction was employed in slab calculations for removing artificial interactions between the slab and its periodic images.

Thermodynamical stability of a surface structure is determined by the surface free energy, $\gamma = G_{\text{slab}} - G_{\text{ref}} - \Delta n_{\text{Ba}}\mu_{\text{Ba}} - \Delta n_{\text{Ti}}\mu_{\text{Ti}} - \Delta n_{\text{O}}\mu_{\text{O}}$, where G_{slab} and G_{ref} are the Gibbs free energies of the slab and the reference system that was selected as the ideal TiO₂-terminated surface. Δn_{Ba} , Δn_{Ti} and Δn_{O} denote the changes in the number of atoms with respect to the reference system. All these quantities correspond to a (2 × 1) surface supercell if not specified otherwise. μ_{Ba} , μ_{Ti} and μ_{O} are the atomic chemical potentials. The accessible boundary of chemical potentials is defined by thermal equilibria between bulk BaTiO₃ and other phases, including bulk Ba, bulk Ti, bulk BaO and bulk TiO₂. Herein we approximated the Gibbs free energy by the DFT total energy, excluding the vibrational contribution. The approximation has been found to be satisfactory for our study: the phase diagram qualitatively remains unchanged when the temperature effect was considered (see Appendix B).

III. RESULTS AND DISCUSSION

At first we exclude the contribution of ferroelectric polarization by fixing the lower three -TiO₂-BaO- bilayers at the cubic bulk structure (i.e., paraelectric phase), as typically done in previous studies^{19,25,26}. In contrast to previous studies, we computed more surface configurations (over 1000) using an advanced evolutionary algorithm²⁷, and obtained many new stable surface structures. Figure 2(a) shows the computed surface phase diagram of BTO(001) for (1 × 1) and (2 × 1) reconstructions, and Fig. 2(b) shows the atomic configurations of the stable phases. It can be seen from Fig. 2(a) that the (1 × 1) ideal BaO-terminated surface is stable at O-rich and Ba-rich conditions. With decreasing μ_{O} and μ_{Ba} , other phases become increasingly more stable. These stable phases include a double-layer TiO₂-termination model (2 × 1)-Ti₂O₄^{19,25}, a TiO adunit model (2 × 1)-TiO formed by adding a TiO unit vertically at the hollow site, and two Ti adatom models, (2 × 1)-Ti and (1 × 1)-Ti, formed by adding a Ti atom at the hollow site in the surface supercell. Note that another double-layer model (1 × 1)-TiO₂ in Fig. 2(b) (not shown in the phase diagram) has surface free energy very close (within ~ 2 meV/Å²) to that of the (2 × 1)-Ti₂O₄ phase. Similar geometrical features of Ti=O titanyl are found in these two thermodynamically degenerate phases.

In experiment, the BTO(001) (2 × 1) surface reconstruction is obtained by Ar⁺ ion sputtering and subsequently annealing native (1 × 1) surface²⁶. Our surface phase diagram suggests three (2 × 1) phases, including the known double-layer model (2 × 1)-Ti₂O₄^{19,25}. Another double-layer (2 × 1) model proposed by previous work²⁶ does not appear in the phase diagram for the reason that it is thermodynamically less stable and its surface free energy is far higher (~ 1.4 eV) than that of the double-layer model (2 × 1)-Ti₂O₄ shown in the phase diagram. Careful analysis of X-ray diffraction data indicates that the (2 × 1) surface has the *p2mm* plane group symmetry²⁶. Based on this information, the (2 × 1)-Ti₂O₄ and (2 × 1)-Ti models that have the *pm* symmetry are excluded. The only remaining (2 × 1) model with the *p2mm* symmetry is (2 × 1)-TiO, which is a thermodynamically stable phase located within the chemical stability ranges of BTO [see Fig. 2(a)]. Interestingly, among over 1000 structures suggested by the evolutionary algorithm, the (2 × 1)-TiO model is the only one that satisfies both conditions of energy and symmetry. We thus attribute the formation of (2 × 1) reconstruction to the addition of TiO units, which is consistent with recent experimental observation of TiO adunits on the *c*(2×2) BTO(001) surface³⁶.

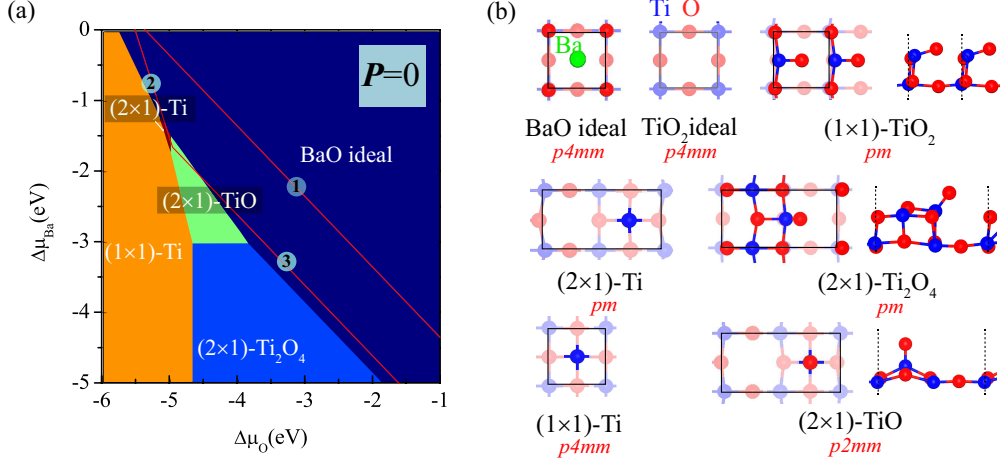


FIG. 2. (Color online) (a) Surface phase diagram of paraelectric BTO(001) for (1×1) and (2×1) reconstructions without the effect of ferroelectric polarization. The red solid lines bound the chemical stability ranges of BTO. The precipitation lines of bulk BaO, Ti and TiO_2 are labeled as 1, 2 and 3, respectively, which bound the accessible chemical potential range defined by thermal equilibria. (b) Schematic atomic structures of stable surface phases. The blue and red balls represent Ti and O atoms, respectively.

We then consider different ferroelectric polarizations (\mathbf{P}_\downarrow and \mathbf{P}_\uparrow) by fixing the lower three $\text{-TiO}_2\text{-BaO-}$ bilayers at the tetragonal bulk structures (ferroelectric phase) as shown in the right panel of Fig. 1. Figure 3 shows the calculated surface phase diagram for two opposite ferroelectric polarization orientations. The interesting $(2 \times 1)\text{-TiO}$ structure remains as a stable phase in the surface phase diagram for both types of polarizations. However, distinct variations of phase diagrams in different polarization conditions can be found, e.g., $(2 \times 1)\text{-TiO}$ is stable in the \mathbf{P}_\downarrow condition over a remarkably extended chemical potential range, while under the \mathbf{P}_\uparrow condition $(2 \times 1)\text{-TiO}$ becomes unstable unless the μ_O is fairly low. The distinction between the phase diagrams under different polarizations indicates that at a certain experimental circumstance (e.g., the oxygen chemical potential is within $-3 \text{ eV} \sim -5 \text{ eV}$), the thermodynamically stable phases are different (i.e., $(2 \times 1)\text{-TiO}$ and (1×1) ideal BaO-terminated surfaces). Thus the external electric field induced ferroelectric switching of the substrate might lead to appearance of different surface structures if kinetic factors were not considered.

To understand this phenomenon, we quantitatively analyze the influence of ferroelectric polarization on the phase diagram by calculating the relative surface Gibbs free energies,

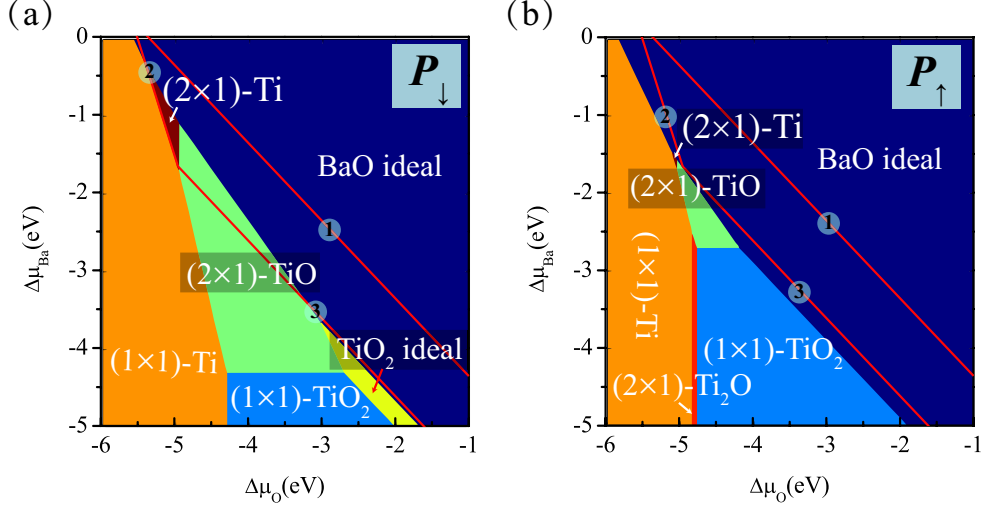


FIG. 3. (Color online) Same as Fig. 2(a) except that the effect of ferroelectric polarization is included. Different ferroelectric polarizations, (a) \mathbf{P}_{\downarrow} and (b) \mathbf{P}_{\uparrow} as illustrated in Fig. 1(b), result in significantly different surface phase diagrams.

$\Delta\gamma(\mathbf{P}_{\downarrow/\uparrow}) = \gamma(\mathbf{P}_{\downarrow/\uparrow}) - \gamma(\mathbf{P}_{=0})$, for various surface structures under two opposite polarization conditions (the case without ferroelectric polarization is taken as the reference). As shown in Table 1, the obtained nonstoichiometric reconstruction phases can be divided into two types: the ones with a TiO_2 overlayer and the other ones with a Ti_xO_y ($y < 2x$) adunit on the primary TiO_2 termination. The surfaces of the “adunit”-type show a considerable energy difference of $\Delta\gamma(\mathbf{P}_{\downarrow}) - \Delta\gamma(\mathbf{P}_{\uparrow})$ ($\sim 1.0 \text{ eV}/(2\times 1)\text{cell}$), indicating significant influence of the ferroelectric polarization on the surface stability. In contrast, the corresponding influence is much smaller for the “overlayer”-type surfaces. Our results of structural relaxation explicitly show that the detailed surface atomic structures of stable phases hardly change with the effect of ferroelectric polarization. Thus, the remarkable difference between $\Delta\gamma(\mathbf{P}_{\downarrow})$ and $\Delta\gamma(\mathbf{P}_{\uparrow})$ does not come from structural relaxation but is mainly caused by electrostatic interactions.

Generally, termination of the spontaneous polarization of ferroelectric materials always gives rise to discontinuity of polarization at surfaces, leading to surface polarization charges (and surface metallicity) whose signs depend on the direction of polarization (see more details in Appendix A). As shown in Figs. 4(a) and 4(b), these surface polarization charges generate a depolarization field (or an internal electric field), whose direction is opposite to that of the polarization. With a constant non-zero depolarization field, the electrostatic en-

TABLE I. Relative surface free energies $[\Delta\gamma]$ and Bader charges for the surface adunits on the TiO_2 termination for the non-stoichiometric phases in different polarization conditions. The case without ferroelectric polarization is taken as the reference of $\Delta\gamma$.

Phase	$\Delta\gamma(\text{eV})$		Charge(e)	
	\mathbf{P}_\downarrow	\mathbf{P}_\uparrow	\mathbf{P}_\downarrow	\mathbf{P}_\uparrow
$(2\times 1)\text{-Ti}_2\text{O}_4$	0.47	0.02	0.03	0.02
$(1\times 1)\text{-TiO}_2$	0.38	-0.09	0.06	-0.02
$(2\times 1)\text{-TiO}$	-0.82	0.32	1.18	1.15
$(2\times 1)\text{-Ti}$	-0.87	0.37	1.46	1.45
$(1\times 1)\text{-Ti}$	-1.00	0.48	2.58	2.59
$(2\times 1)\text{-Ti}_2\text{O}$	-0.77	0.17	1.50	1.53

ergy of ferroelectric surfaces would diverge with increasing thickness. Such an electrostatic instability, however, can be eliminated by compensating the depolarization field through various mechanisms, like introducing an external electric voltage^{37,38}, surface adsorption or surface reconstruction. For the intrinsic mechanism of surface reconstruction, the compensation of the depolarization field depends significantly on the direction of polarization, leading to distinct surface free energies $\Delta\gamma(\mathbf{P}_\downarrow)$ and $\Delta\gamma(\mathbf{P}_\uparrow)$.

Different surface reconstructions result in different surface electrostatic potentials and thus correspond to varying surface dipoles. For a specified surface reconstruction, if the depolarization field is compensated by the surface dipole [see Figs. 4(c) and 4(d)], the electrostatic energy would get lowered by this compensation and the whole system thus gets stabilized. In contrast, reversing the depolarization field would yield higher electrostatic energy and larger surface free energy. This could well explain the polarization dependent behaviors, as demonstrated below. While the magnitude of surface dipole is not easy to quantify, a qualitative analysis is possible for the present system, considering that the normal oxidation states of Ti and O are +4 and -2, respectively.

For the so-called ‘‘adunit’’-type surfaces, the adunit that has Ti/O ratio larger than 1/2 is chemically unsaturated. When the adunit binds with the substrate, electron transfer from the adunit to the substrate occurs, resulting in a positively charged adunit as shown in Fig. 4(c). For the \mathbf{P}_\downarrow condition, the charge transfer decreases the surface polarization charge

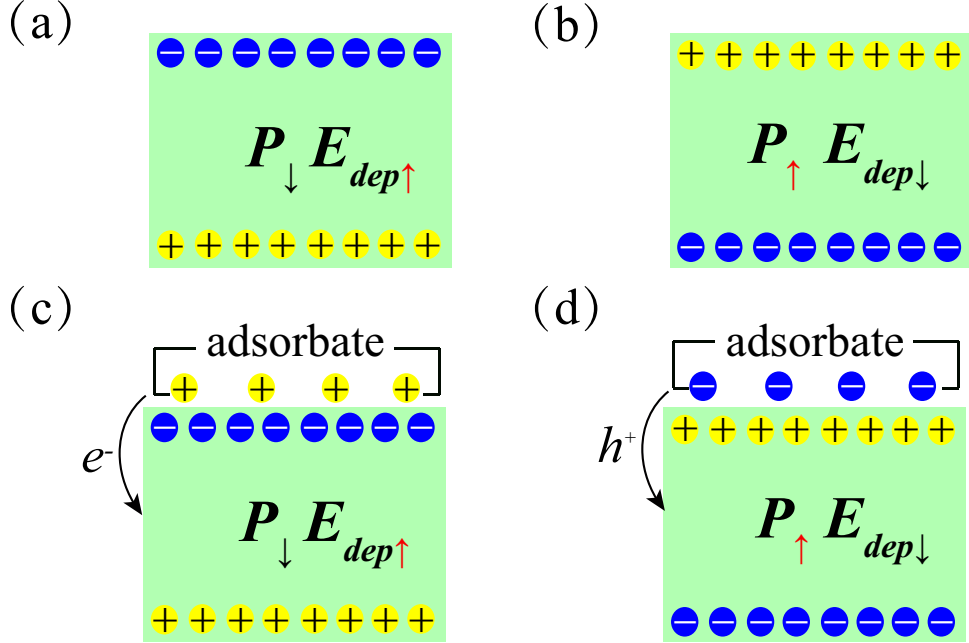


FIG. 4. (Color online) (a)/(b) The discontinuity of ferroelectric polarization ($\mathbf{P}_{\downarrow}/\mathbf{P}_{\uparrow}$) at the surface induces surface polarization charges, resulting in a depolarization field opposite to the direction of polarization. (c)/(d) Schematic of ionic surface compensation mechanism. Charge transfer between the adsorbate and substrate induces a surface dipole, which compensates the depolarization field and thus lowers the electrostatic energy of the system, leading to lower surface free energy.

and the charge-transfer induced dipole compensates the depolarization field, resulting in a negative $\Delta\gamma(\mathbf{P}_{\downarrow})$. We denote such a charge-transfer induced compensation as the ionic surface compensation mechanism, as used in previous work³⁹. The effect gets inverted for the \mathbf{P}_{\uparrow} condition, leading to a positive $\Delta\gamma(\mathbf{P}_{\uparrow})$. All these features are consistent with the calculation data (see Table 1). To analyze the results in more details, we present the calculated Bader charges in Table 1. Due to the lower coordination number of surface atoms, the calculated charge of the adunits, e.g., TiO, which have formed Ti=O double-bonded titanyl groups, is about +1.18e. A large surface free energy difference of “adunit”-type phases [> 1.0 eV/(2 \times 1)cell] is induced through the ionic surface compensation mechanism described above. The detailed spatial distribution of charge transfer is given in Appendix A.

For the so-called “overlayer”-type phases in which the overlayer itself is chemically saturated, there exists tiny charge transfer between the overlayer and the substrate (see Table 1), suggesting that the effect of ionic surface charge compensation is negligible. The atomic

rumpling of TiO₂ overlayer, with the O atoms at the surface all above the Ti atoms, contributes a downward surface dipole $\mathbf{P}_s(\downarrow)$. Such a kind of structural rumpling has also been predicted for the bare surfaces of perovskites which can lead to a relatively low catalytic activity of the surface⁴¹. The anti-parallel/parallel configuration of the \mathbf{P}_s to the \mathbf{P}_\uparrow and \mathbf{P}_\downarrow of the substrate leads to the stabilization/destabilization scenarios, respectively. Thus, the polarization to the surface is suppressed for the \mathbf{P}_\uparrow condition but enhanced for \mathbf{P}_\downarrow condition, resulting in the higher $\Delta\gamma$. The resulting changes of electrostatic potential alignment and the surface electronic structure by different types of reconstruction are given in Appendix A. The obtained (2×1)-TiO surface shows n type metallicity in both polarization conditions.

It should be noticed that the contributions of charge transfer and structural rumpling are strongly entangled and cannot be clearly distinguished by direct calculations, especially in the “adunit”-type phases like (2×1)-TiO. Nevertheless, compared to the relatively smaller $[\Delta\gamma(\mathbf{P}_\downarrow) - \Delta\gamma(\mathbf{P}_\uparrow)]$ of (1×1)-TiO₂ case (~ 0.4 eV) which is basically contributed by the structural rumpling, the considerably larger $[\Delta\gamma(\mathbf{P}_\downarrow) - \Delta\gamma(\mathbf{P}_\uparrow)]$ of (2×1)-TiO case (~ -1.1 eV) can be mainly attributed to charge transfer (i.e., the ionic surface compensation mechanism).

The above results as well as related physical mechanism clearly indicate that the ferroelectric polarization plays a significant role in the surface stability of ferroelectric materials. This reveals a new degrees of freedom to affect the growth of the surface: in addition to tuning the growth condition, e.g., substrate temperature and partial pressure of source, it is convenient and feasible to control the surface stability by applying an external electric field.

IV. CONCLUSIONS

In summary, we have constructed the surface phase diagram of (2×1) and (1×1) BTO(001) reconstructions by employing a surface structure prediction method based on evolutionary algorithm and exploring over 1000 candidate structures. We predict a surface phase diagram containing many new surface structures, including a thermodynamically stable (2×1)-TiO phase that has the $p2mm$ plane group symmetry as observed experimentally. Critically, the ferroelectric polarization has been included as a new parameter of surface structure prediction. We find the surface phase diagram changes significantly with varying ferroelectric polarization due to the ionic surface compensation mechanism. The

distinguishing feature of ferroelectrics is the polarization switching upon applying external electric field, thus the control over surface stability is feasible by applying electric field. The underlying physical mechanism is expected to be quite general. Our results may help in tuning surface structures and properties of ferroelectric materials.

ACKNOWLEDGMENTS

We thank Zhirong Liu and Xiangfeng Zhou for valuable discussions. We acknowledge the support of the Ministry of Science and Technology of China (Grant Nos. 2011CB921901 and 2011CB606405), and the National Natural Science Foundation of China. A.R.O. thanks the National Science Foundation (EAR-1114313, DMR-1231586), DARPA (Grants No. W31P4Q1210008 and No. W31P4Q1310005), the Government (No. 14.A12.31.0003) and the Ministry of Education and Science of Russian Federation (Project No. 8512) for financial support, and Foreign Talents Introduction and Academic Exchange Program (No. B08040).

Appendix A: Electronic Structure

In the ferroelectric thin film, the local bands are shifted by the electrostatic potential. When the accumulated electrostatic potential exceeds the energy gap of the bulk phase, a charge redistribution takes place, leading to the compensating surface charges and the surface metallization, as schematized in Fig. A.1(a). Our calculated layer-projected density of states (DOS) of the BaTiO₃ slab without surface reconstruction [Fig. A.1(b)] is consistent with this general picture. Due to the charge transfer, the ideal surface, either BaO- or TiO₂-terminated surface becomes metallic. The surface metallicity, more specifically, can be regarded as n and p types for the \mathbf{P}_\uparrow and \mathbf{P}_\downarrow conditions, respectively [Fig. A.1(c), (d)]. Compared to ideal TiO₂-terminated surface, the relatively lower density of states around the Fermi level indicate the weaker metallicity of ideal BaO-terminated surface.

To reveal the effects of surface reconstruction on the electrostatic stability, we have calculated the resulting spatial distribution of electrostatic potential, by taking the energy level of Ti 3s orbital in each bulk-like cells as the reference of the potential Φ , as shown in Fig. A.2. Neutral TiO₂-overlayer-type phases retain the features of the ideal TiO₂-terminated slab that the electrostatic potential keep increasing/decreasing from the bottom layer. Figure. A.3

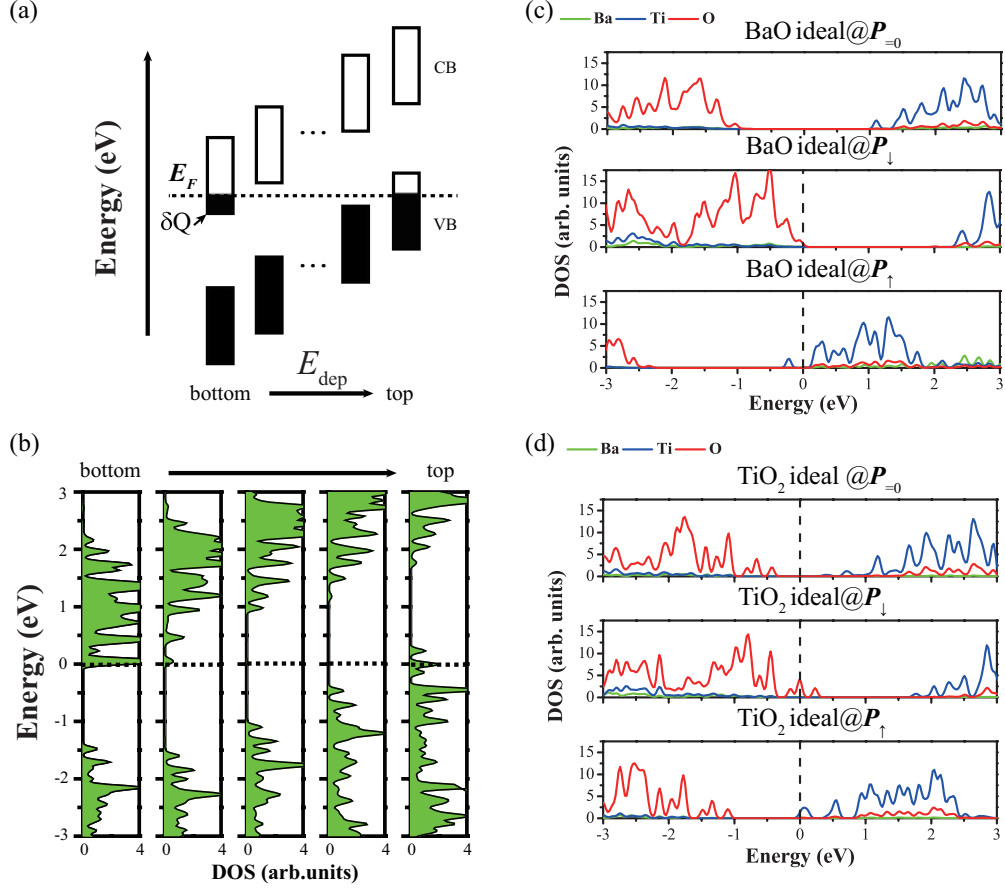


FIG. A.1. (Color online) (a) Schematic of the electronic structure of ferroelectric thin film. The overall gap is closed due to electrostatic potential accumulation by the depolarization field. Here δQ denotes the charge transfer from the top layer to the bottom layer. (b) Calculated layer resolved density of states (DOS) of ideal TiO_2 -terminated BaTiO_3 slab in the \mathbf{P}_\downarrow condition. (c)/(d) Calculated surface DOS of ideal BaO -/ TiO_2 -terminated BaTiO_3 slab in different polarization conditions. The Fermi level is set at zero.

shows calculated layer-resolved charge transfer of BaTiO_3 slabs with different surface configurations. In the \mathbf{P}_\downarrow condition, the charge transfer [Fig. A.3(b)] induced by the TiO adunit produces an electric field opposite to the depolarization field, strongly reducing the potential accumulation at the surface. However, in the \mathbf{P}_\uparrow condition the scenario is different, the TiO -adunit induced electric field is along the direction of the depolarization field, enhancing the potential accumulation at the surface. The results of the calculated enhancement/reduction of the surface potential are in good agreement with the calculated relative surface energies.

Fig. A.4 shows the calculated surface DOS of the stable phases, (2×1) - TiO and (1×1) -

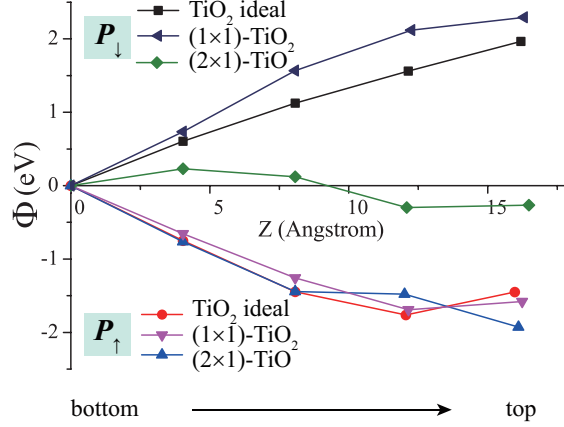


FIG. A.2. (Color online) The relative electrostatic potential Φ of BaTiO_3 slabs with different surface configurations. The Φ of the bottom layer of the slab is taken as the reference zero.

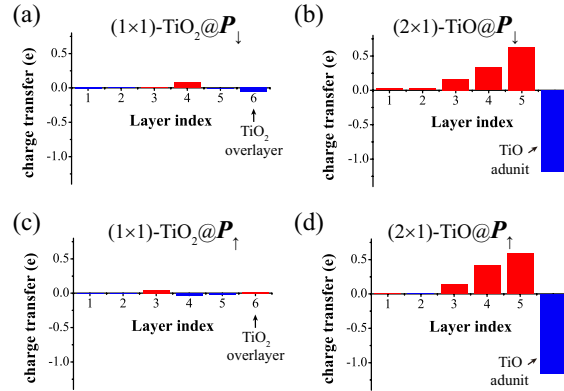


FIG. A.3. (Color online) Calculated layer-resolved charge transfer of BaTiO_3 slabs with different surface configurations (red and blue represent electron accumulation and depletion, respectively).

TiO_2 in the different polarization conditions. For the (1×1) - TiO_2 cases, the electronic structure of the surface remains almost unchanged compared to the ideal TiO_2 -terminated surface. For the (2×1) - TiO case in the \mathbf{P}_\downarrow condition, along with the strong reduction of the electrostatic potential accumulation and charge transfer effect, the significant change in the surface electronic structure can be found, i.e., from the p -type metallicity to the n -type metallicity.

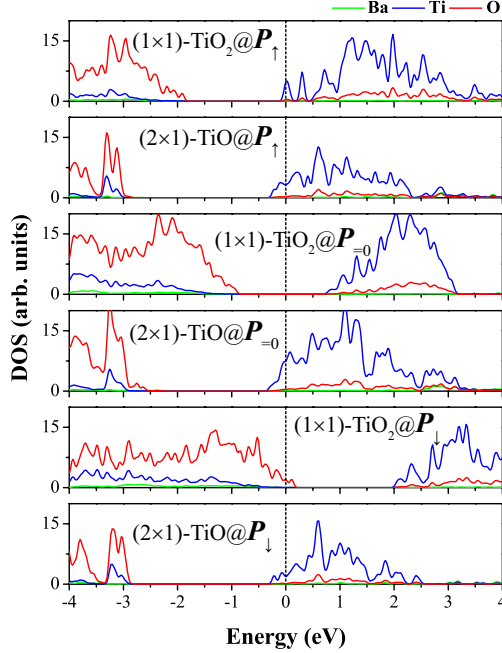


FIG. A.4. (Color online) Calculated surface DOS of representative phases, i.e., (2×1) -TiO and (1×1) -TiO₂, in the different polarization conditions. Ti-, Ba- and O-resolved DOS are shown in blue, green and red lines, respectively.

Appendix B: The temperature effect

Following the approach of Reuter and Scheffler⁶, the temperature-dependent Gibbs free energy of the slab is approximated by the sum of DFT total energy at zero temperature and the vibration energy at finite temperature, neglecting the pV term ($\sim 10^{-3}$ meV/Å²). In turn, the Gibbs free energy of the slab is written as

$$G_{\text{slab}} = E^{\text{DFT}}(\text{slab}) + F^{\text{VIB}}(\text{slab}). \quad (\text{B1})$$

Generally the vibration energy contribution can be obtained within the harmonic approximation by calculating the phonon dispersion⁴². However, as the large amount of computation, it is difficult to calculate the phonon dispersion of the whole slab. Note that only the relative surface free energy is meaningful to the determination of the phase diagram. The principal difference of the slabs comes from the different surface adsorbates. In this regard, we can approximate the vibration energy contribution using the Einstein model by calculating the vibration frequencies of the surface adsorbates of different surface structures. Then the

vibration energy can be written as

$$F^{\text{VIB}}(T, \omega) = \frac{\hbar\omega}{2} + kT \ln(1 - e^{-\frac{\hbar\omega}{kT}}) \quad (\text{B2})$$

where T and ω represent, respectively, the temperature of the system and the characteristic vibration frequency for the phonon modes. We use the finite displacement method to calculate the vibration frequency. The force constant matrix \mathbf{K} is generated by calculating the force \mathbf{F} of the atoms with the finite atomic displacement \mathbf{X} applied,

$$\mathbf{F} = \begin{pmatrix} K_{xx} & K_{xy} & K_{xz} \\ K_{yx} & K_{yy} & K_{yz} \\ K_{zx} & K_{zy} & K_{zz} \end{pmatrix} \mathbf{X} \quad (\text{B3})$$

and the vibration frequency is

$$\omega_i = \sqrt{\frac{K_i}{m_{\text{atom}}}} \quad (\text{B4})$$

where i represents the vibration mode, K_i is the i -th eigenvalue of the force constant matrix, and m_{atom} is the atomic mass. Table B.1 just lists the calculated average characteristic vibration frequency and the total vibrational free energy at 1100 K of surface adsorbates of different stable phases involved in the 0 K phase diagram.

Due to the requirement for the surface to be in equilibrium with the bulk barium titanate and to keep barium, titanium and oxygen atoms from precipitating on the surface, the accessible chemical potential boundary conditions go to,

$$\mu_{\text{Ba}} + \mu_{\text{Ti}} + 3\mu_{\text{O}} = g_{\text{BaTiO}_3}^{\text{Bulk}}(T, p) \quad (\text{B5})$$

$$\mu_{\text{Ba}} \leq g_{\text{Ba}}^{\text{Bulk}}(T, p) \quad (\text{B6})$$

$$\mu_{\text{Ti}} \leq g_{\text{Ti}}^{\text{Bulk}}(T, p) \quad (\text{B7})$$

$$\mu_{\text{Ba}} + \mu_{\text{O}} \leq g_{\text{BaO}}^{\text{Bulk}}(T, p) \quad (\text{B8})$$

$$\mu_{\text{Ti}} + 2\mu_{\text{O}} \leq g_{\text{TiO}_2}^{\text{Bulk}}(T, p) \quad (\text{B9})$$

where $g^{\text{Bulk}}(T, p)$ is the Gibbs free energy of corresponding compounds. For solid phase compounds, temperature dependent $g^{\text{Bulk}}(T, p)$ can be approximated with the sum of 0 K total energy ($E_{\text{Bulk}}^{\text{DFT}}$) obtained from DFT calculation and vibrational energy ($F_{\text{Bulk}}^{\text{VIB}}(T, p)$) at finite temperature computed within the harmonic approximation, using the PHONOPY package⁴². An energy correction has been applied to the μ_{O} by taking the reference of

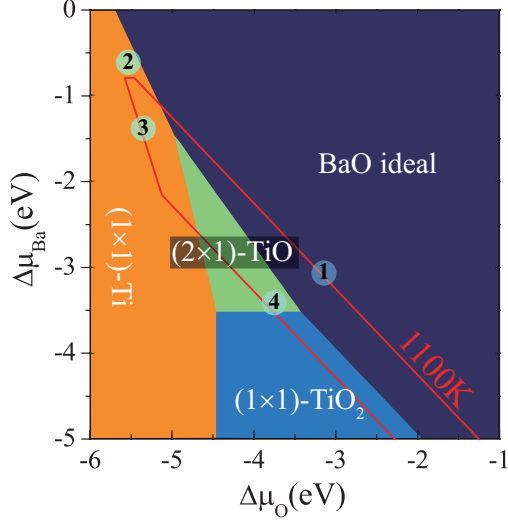


FIG. B.1. (Color online) Surface phase diagram of $\text{BaTiO}_3(001)$ for (1×1) and (2×1) reconstructions in the \mathbf{P}_\downarrow condition. The vibration contribution is included. The red solid lines bound the chemical stability ranges of BaTiO_3 . The precipitation lines of bulk BaO, Ba, Ti and TiO_2 are labeled as 1-4, respectively, which bound the accessible chemical potential range defined by thermal equilibria at 1100 K.

experimental data of Gibbs free energy of formation of BaTiO_3 , BaO and TiO_2 ^{43–45}. The calculated data are listed in Table B.1.

Fig. B.1 shows the surface phase diagram at 1100 K with the vibration contribution included. Compared to the phase diagram in Fig. 2(a) at zero temperature, the accessible chemical potential boundaries are slightly shifted. However, the thermodynamically stable phase is still (2×1) -TiO and the overall pattern of the calculated phase diagram does not change upon adding the vibration contribution. This shows that the temperature effect is negligible in the present case.

* dwh@phys.tsinghua.edu.cn

¹ U. Diebold, Surf. Sci. Rep. **48**, 53 (2003).

² S. M. Young and A. M. Rappe, Phys. Rev. Lett. **109**, 116601 (2012).

³ K. Garrity, A. Kakekhani, A. Kolpak, and S. Ismail-Beigi, Phys. Rev. B **88**, 045401 (2013).

⁴ Y. Xu, O. T. Hofmann, R. Schlesinger, S. Winkler, J. Frisch, J. Niederhausen, A. Vollmer,

TABLE B.1. Calculated average characteristic vibration frequency and total vibrational free energy at 1100 K of surface adsorbates of different stable phases involved in the 0 K phase diagram.

Phase	Atom	$\bar{\omega}$ (cm^{-1})	$F_{\text{total}}^{\text{vib}}$ (1100 K) (eV)
(2×1)-Ti ₂ O ₄	Ti ₁	325	-0.245
	Ti ₂	317	-0.267
	O ₁	491	-0.248
	O ₂	385	-0.200
	O ₃	550	-0.110
	O ₄	422	-0.166
(1×1)-TiO ₂	Ti ₁	336	-0.236
	O ₁	374	-0.232
	O ₂	428	-0.166
(2×1)-TiO	Ti ₁	382	-0.215
	O ₁	420	-0.264
(2×1)-Ti	Ti ₁	258	-0.311
(1×1)-Ti	Ti ₁	247	-0.324
	Ti ₂	247	-0.324
(2×1)-Ti ₂ O	Ti ₁	236	-0.345
	Ti ₂	324	-0.243
	O ₁	372	-0.223
BaO ideal	Ba ₁	103	-0.58
	O ₁	331	-0.249

S. Blumstengel, F. Henneberger, N. Koch, P. Rinke, and M. Scheffler, Phys. Rev. Lett. **111**, 226802 (2013).

⁵ A. Kakekhani and S. Ismail-Beigi, ACS Catal. **5**, 4537 (2015).

⁶ K. Reuter and M. Scheffler, Phys. Rev. B **65**, 035406 (2001).

⁷ B. Meyer, Phys. Rev. B **69**, 045416 (2004).

⁸ R. Eglitis and D. Vanderbilt, Phys. Rev. B **76**, 155439 (2007).

TABLE B.2. Calculated and experimental Gibbs free energy of formation $\Delta_f G^0$ of various compounds (in units of eV).

Compound	Cal.	Exp.
BaTiO ₃ (tetragonal)	-16.29	-16.29 ⁴⁴
TiO ₂ (anatase)	-9.79	-9.25 ⁴⁵
BaO	-5.25	-5.36 ⁴⁵

- ⁹ S. V. Levchenko and A. M. Rappe, *Phys. Rev. Lett.* **100**, 256101 (2008).
- ¹⁰ R. Ramesh and N. A. Spaldin, *Nat. Mat.* **6**, 21 (2007).
- ¹¹ H. Zheng, J. Wang, S. Lofland, Z. Ma, L. Mohaddes-Ardabili, T. Zhao, L. Salamanca-Riba, S. Shinde, S. Ogale, F. Bai, D. Viehland, Y. Jia, D. G. Schlom, M. Wuttig, A. Roytburd, and R. Ramesh, *Science* **303**, 661 (2004).
- ¹² S. Hontsu, J. Ishii, H. Tabata, and T. Kawai, *Appl. Phys. Lett.* **67**, 554 (1995).
- ¹³ C.-G. Duan, S. S. Jaswal, and E. Y. Tsymlal, *Phys. Rev. Lett.* **97**, 047201 (2006).
- ¹⁴ L. Bocher, A. Gloter, A. Crassous, V. Garcia, K. March, A. Zobelli, S. Valencia, S. Enouz-Vedrenne, X. Moya, N. D. Marthur, C. Deranlot, S. Fusil, K. Bouzeshouane, M. Bibes, A. Barthélémy, C. Colliex, and O. Stéhan, *Nano Lett.* **12**, 376 (2011).
- ¹⁵ J. Yu, Z. Wu, Z. Liu, Q. Yan, J. Wu, and W. Duan, *J. Phys.: Condens. Matter* **20** (2008).
- ¹⁶ M. Li, Y. Gu, Y. Wang, L.-Q. Chen, and W. Duan, *Phys. Rev. B* **90**, 054106 (2014).
- ¹⁷ P. G, P. Aguado-Puente, and J. Junquera, *Phys. Rev. B* **87**, 085305 (2013).
- ¹⁸ Y. L. Li, L. E. Cross, and L. Q. Chen, *J. Appl. Phys.* **98**, 064101 (2005).
- ¹⁹ A. M. Kolpak, D. Li, R. Shao, A. M. Rappe, and D. A. Bonnell, *Phys. Rev. Lett.* **101**, 036102 (2008).
- ²⁰ H. Bando, T. Shimitzu, Y. Aiura, Y. Haruyama, K. Oka, and Y. Nishihara, *J. Vac. Sci. & Tech. B* **14**, 1060 (1996).
- ²¹ T. Shimizu and H. B. A. H. O. Nishihara, *Jpn. J. Appl. Phys.* **34**, L1305 (1995).
- ²² L. Hudson, R. Kurtz, S. Robey, D. Temple, and R. Stockbauer, *Phys. Rev. B* **47**, 10832 (1993).
- ²³ C. Hagendorf, K.-M. Schindler, T. Doege, and H. Neddermeyer, *Appl. Surf. Sci.* **142**, 106 (1999).
- ²⁴ J. M. P. Martirez, E. H. Morales, W. A. Saidi, D. A. Bonnell, and A. M. Rappe, *Phys. Rev.*

- Lett. **109**, 256802 (2012).
- ²⁵ N. Iles, F. Finocchi, and K. D. Khodja, *J. Phys.: Condens. Matter* **22**, 305001 (2010).
- ²⁶ H. Meyerheim, A. Ernst, K. Mohseni, I. Maznichenko, S. Ostanin, F. Klimenta, N. Jedrecy, W. Feng, I. Mertig, R. Felici, and J. Kirschner, *Phys. Rev. Lett.* **108**, 215502 (2012).
- ²⁷ Q. Zhu, L. Li, A. R. Oganov, and P. B. Allen, *Phys. Rev. B* **87**, 195317 (2013).
- ²⁸ G. Kresse and J. Furthmüller, *Phys. Rev. B* **54**, 11169 (1996).
- ²⁹ G. Kresse and D. Joubert, *Phys. Rev. B* **59**, 1758 (1999).
- ³⁰ J. P. Perdew, K. Burke, and M. Ernzerhof, *Phys. Rev. Lett.* **77**, 3865 (1996).
- ³¹ PBE functional is used for its overall good description of the cohesive energies of all compounds involved (bulk: Ba, Ti, BaO, TiO₂ and BaTiO₃; molecule: O₂). It is worth noting that GGA functionals might overestimate the equilibrium volume of paraelectric and ferroelectric phases of BaTiO₃. Therefore we have used the experimental lattice constants of $a = 3.991 \text{ \AA}$, $c = 4.035 \text{ \AA}$ for tetragonal phase [G. H. Kwei, A. C. Lawson, S. J. L. Billinge, and S. W. Cheong, *J. Phys. Chem.* **97**, 2368 (1993).] and $a = 4.01 \text{ \AA}$ for cubic phase [K. H. Hellwege and A. M. Hellwege (Eds.), *Ferroelectrics and Related Substances*, New Series Vol. 3, Landolt-Bornstein (Springer, Berlin, 1969) (group III)]. Our calculations well reproduce the atomic distortions and polarization of experiments (cal.: $0.29\text{C}/\text{m}^2$, exp.: $0.27\text{C}/\text{m}^2$). Further test calculations using PBEsol functional [J. P. Perdew, A. Ruzsinszky, G. I. Csonka, O. A. Vydrov, G. E. Scuseria, L. A. Constantin, X. Zhou, and K. Burke, *Phys. Rev. Lett.* **100**, 136406 (2008).] show negligible affection on the results.
- ³² A. R. Oganov and C. W. Glass, *J. Chem. Phys.* **124**, 244704 (2006).
- ³³ X.-F. Zhou, A. R. Oganov, X. Shao, Q. Zhu, and H.-T. Wang, *Phys. Rev. Lett.* **113**, 176101 (2014).
- ³⁴ Q. Wang, A. R. Oganov, Q. Zhu, and X.-F. Zhou, *Phys. Rev. Lett.* **113**, 266101 (2014).
- ³⁵ The selection of the bottom surface termination (i.e., TiO₂- or BaO- terminated bottom surface) has been found not to affect the results. We have also performed test calculations on the slab thickness effect by adding extra unit cell to the slab, which yield very close relative surface free energies and the same surface stability.
- ³⁶ E. H. Morales, J. M. P. Martirez, W. A. Saidi, A. M. Rappe, and D. A. Bonnell, *ACS Nano* **8**, 4465 (2014).
- ³⁷ M. Stengel, D. Vanderbilt, and N. A. Spaldin, *Phys. Rev. B* **80**, 224110 (2009).

- ³⁸ M. Stengel, N. A. Spaldin, and D. Vanderbilt, *Nat. Phys.* **5**, 304 (2009).
- ³⁹ G. B. Stephenson and M. J. Highland, *Phys. Rev. B* **84**, 064107 (2011).
- ⁴⁰ M. Stengel, *Phys. Rev. B* **84**, 205432 (2011).
- ⁴¹ M. Fechner, S. Ostanin, and I. Mertig, *Phys. Rev. B* **77**, 094112 (2008).
- ⁴² A. Togo, F. Oba, and I. Tanaka, *Phys. Rev. B* **78**, 134106 (2008).
- ⁴³ K. Johnston, M. R. Castell, A. T. Paxton, and M. W. Finnis, *Phys. Rev. B* **70**, 085415 (2004).
- ⁴⁴ J. A. Dean, *Lange's Handbook of Chemistry, 12th ed* (McGraw-Hill Book Company, New York, NY, 1979).
- ⁴⁵ M. Binnewies and E. Milke, *Thermochemical Data of Elements and Compounds* (Wiley-VCH Verlag GmbH, 2008), ISBN 9783527618347, URL <http://dx.doi.org/10.1002/9783527618347.ch5a>.